Measurement of inclusive jet cross section and substructure in $p+p$ collisions at $\sqrt{s}=200$ GeV

N. J. Abdulameer,[15,23] U. Acharya,[19] C. Aidala,[39,45] N. N. Ajitanand,[66,*] Y. Akiba,[61,62,†] R. Akimoto,[11] J. Alexander,[66] M. Alfred,[22] V. Andrieux,[45] S. Antsupov,[64] K. Aoki,[32,61] N. Apadula,[28,67] H. Asano,[35,61] E. T. Atomssa,[67] T. C. Awes,[56] B. Azmoun,[7] V. Babintsev,[24] M. Bai,[6] X. Bai,[10] N. S. Bandara,[43] B. Bannier,[67] E. Bannikov,[64] K. N. Barish,[8] S. Bathe,[5,62] V. Baublis,[59] C. Baumann,[7] S. Baumgart,[61] A. Bazilevsky,[7] M. Beaumier,[8] R. Belmont,[12,54] A. Berdnikov,[64] Y. Berdnikov,[64] L. Bichon,[73] D. Black,[8] B. Blankenship,[73] D. S. Blau,[34,51] J. S. Bok,[53] V. Borisov,[64] K. Boyle,[62] M. L. Brooks,[39] J. Bryslawskyj,[5,8] H. Buesching,[7] V. Bumazhnov,[24] S. Butsyk,[52] S. Campbell,[13,28] R. Cervantes,[67] C.-H. Chen,[62] D. Chen,[67] M. Chiu,[7] C. Y. Chi,[13] I. J. Choi,[25] J. B. Choi,[30,*] S. Choi,[65] P. Christiansen,[40] T. Chujo,[71] V. Cianciolo,[56] Z. Citron,[74] B. A. Cole,[13] M. Connors,[19,62] R. Corliss,[67] N. Cronin,[47,67] N. Crossette,[47] M. Csanád,[16] T. Csörgő,[44,75] L. D'Orazio,[42] T. W. Danley,[55] A. Datta,[52] M. S. Daugherity,[1] G. David,[7,67] K. DeBlasio,[52] K. Dehmelt,[67] A. Denisov,[24] A. Deshpande,[62,67] E. J. Desmond,[7] L. Ding,[28] A. Dion,[67] D. Dixit,[67] V. Doomra,[67] J. H. Do,[76] O. Drapier,[36] A. Drees,[67] K. A. Drees,[6] J. M. Durham,[39] A. Durum,[24] H. En'yo,[61,62] T. Engelmore,[13] A. Enokizono,[61,63] R. Esha,[67] K. O. Eyser,[7] B. Fadem,[47] W. Fan,[67] N. Feege,[67] D. E. Fields,[52] M. Finger, Jr.,[9] M. Finger,[9] D. Firak,[15,67] D. Fitzgerald,[45] F. Fleuret,[36] S. L. Fokin,[34] J. E. Frantz,[55] A. Franz,[7] A. D. Frawley,[18] Y. Fukao,[32] Y. Fukuda,[71] T. Fusayasu,[49] K. Gainey,[1] P. Gallus,[14] C. Gal,[67] P. Garg,[3,67] A. Garishvili,[69] I. Garishvili,[38] H. Ge,[67] F. Giordano,[25] A. Glenn,[38] X. Gong,[66] M. Gonin,[36] Y. Goto,[61,62] R. Granier de Cassagnac,[36] N. Grau,[2] S. V. Greene,[73] M. Grosse Perdekamp,[25] T. Gunji,[11] T. Guo,[67] H. Guragain,[19] Y. Gu,[66] T. Hachiya,[61,62] J. S. Haggerty,[7] K. I. Hahn,[17] H. Hamagaki,[11] H. F. Hamilton,[1] J. Hanks,[67] S. Y. Han,[17,33] S. Hasegawa,[29] T. O. S. Haseler,[19] K. Hashimoto,[61,63] R. Hayano,[11] T. K. Hemmick,[67] T. Hester,[8] X. He,[19] J. C. Hill,[28] K. Hill,[12] A. Hodges,[19,25] R. S. Hollis,[8] K. Homma,[21] B. Hong,[33] T. Hoshino,[21] N. Hotvedt,[28] J. Huang,[7,39] T. Ichihara,[61,62] Y. Ikeda,[61] K. Imai,[29] Y. Imazu,[61] M. Inaba,[71] A. Iordanova,[8] D. Isenhower,[1] A. Isinhue,[47] D. Ivanishchev,[59] S. J. Jeon,[48] M. Jezghani,[19] X. Jiang,[39] Z. Ji,[67] B. M. Johnson,[7,19] K. S. Joo,[48] D. Jouan,[57] D. S. Jumper,[25] J. Kamin,[67] S. Kanda,[11,32] B. H. Kang,[20] J. H. Kang,[76] J. S. Kang,[20] D. Kapukchyan,[8] J. Kapustinsky,[39] S. Karthas,[67] D. Kawall,[43] A. V. Kazantsev,[34] J. A. Key,[52] V. Khachatryan,[67] P. K. Khandai,[3] A. Khanzadeev,[59] K. M. Kijima,[21] C. Kim,[8,33] D. J. Kim,[31] E.-J. Kim,[30] M. Kim,[65] Y.-J. Kim,[25] Y. K. Kim,[20] D. Kincses,[16] E. Kistenev,[7] J. Klatsky,[18] D. Kleinjan,[8] P. Kline,[67] T. Koblesky,[12] M. Kofarago,[16,75] B. Komkov,[59] J. Koster,[62] D. Kotchetkov,[55] D. Kotov,[59,64] L. Kovacs,[16] F. Krizek,[31] S. Kudo,[71] K. Kurita,[63] M. Kurosawa,[61,62] Y. Kwon,[76] Y. S. Lai,[13] J. G. Lajoie,[28,56] A. Lebedev,[28] D. M. Lee,[39] G. H. Lee,[30] J. Lee,[17,68] K. B. Lee,[39] K. S. Lee,[33] S. Lee,[76] S. H. Lee,[28,67] M. J. Leitch,[39] M. Leitgab,[25] Y. H. Leung,[67] B. Lewis,[67] S. H. Lim,[39,60,76] M. X. Liu,[39] X. Li,[10] X. Li,[39] V.-R. Loggins,[25] S. Lokos,[16] D. A. Loomis,[45] K. Lovasz,[15] D. Lynch,[7] C. F. Maguire,[73] T. Majoros,[15] Y. I. Makdisi,[6] M. Makek,[74,77] A. Manion,[67] V. I. Manko,[34] E. Mannel,[7] M. McCumber,[12,39] P. L. McGaughey,[39] D. McGlinchey,[12,18,39] C. McKinney,[25] A. Meles,[53] M. Mendoza,[8] B. Meredith,[25] Y. Miake,[71] T. Mibe,[32] A. C. Mignerey,[42] A. Milov,[74] D. K. Mishra,[4] J. T. Mitchell,[7] M. Mitrankova,[64,67] Iu. Mitrankov,[64,67] G. Mitsuka,[32,62] S. Miyasaka,[61,70] S. Mizuno,[61,71] A. K. Mohanty,[4] S. Mohapatra,[66] P. Montuenga,[25] T. Moon,[33,76] D. P. Morrison,[7] M. Moskowitz,[47] T. V. Moukhanova,[34] B. Mulilo,[33,61,78] T. Murakami,[35,61] J. Murata,[61,63] A. Mwai,[66] T. Nagae,[35] K. Nagai,[70] S. Nagamiya,[32,61] K. Nagashima,[21] T. Nagashima,[63] J. L. Nagle,[12] M. I. Nagy,[16] I. Nakagawa,[61,62] Y. Nakamiya,[21] K. R. Nakamura,[35,61] T. Nakamura,[61] K. Nakano,[61,70] C. Nattrass,[69] P. K. Netrakanti,[4] M. Nihashi,[21,61] T. Niida,[71] R. Nouicer,[7,62] N. Novitzky,[31,67] T. Novák,[44,75] G. Nukazuka,[61,62] A. S. Nyanin,[34] E. O'Brien,[7] C. A. Ogilvie,[28] H. Oide,[11] K. Okada,[62] J. D. Orjuela Koop,[12] M. Orosz,[15,23] J. D. Osborn,[45,56] A. Oskarsson,[40] G. J. Ottino,[52] K. Ozawa,[32,71] R. Pak,[7] V. Pantuev,[26] V. Papavassiliou,[53] I. H. Park,[17,68] J. S. Park,[65] S. Park,[46,61,65,67] S. K. Park,[33] L. Patel,[19] M. Patel,[28] S. F. Pate,[53] J.-C. Peng,[25] D. V. Perepelitsa,[7,12,13] G. D. N. Perera,[53] D. Yu. Peressounko,[34] C. E. PerezLara,[67] J. Perry,[28] R. Petti,[7,67] M. Phipps,[7,25] C. Pinkenburg,[7] R. P. Pisani,[7] M. Potekhin,[7] M. L. Purschke,[7] H. Qu,[1] J. Rak,[31] I. Ravinovich,[74] K. F. Read,[56,69] D. Reynolds,[66] V. Riabov,[51,59] Y. Riabov,[59,64] E. Richardson,[42] D. Richford,[5,72] T. Rinn,[28] N. Riveli,[55] D. Roach,[73] S. D. Rolnick,[8] M. Rosati,[28] Z. Rowan,[5] M. S. Ryu,[20] A. S. Safonov,[64] B. Sahlmueller,[67] N. Saito,[32] T. Sakaguchi,[7] H. Sako,[29] V. Samsonov,[51,59] M. Sarsour,[19] S. Sato,[29] S. Sawada,[32] B. Schaefer,[73] B. K. Schmoll,[69] K. Sedgwick,[8] J. Seele,[62] R. Seidl,[61,62] Y. Sekiguchi,[11] A. Seleznev,[64] A. Sen,[19,28,69] R. Seto,[8] P. Sett,[4] A. Sexton,[42] D. Sharma,[67] A. Shaver,[28] I. Shein,[24] Z. Shi,[39] T.-A. Shibata,[61,70] K. Shigaki,[21] M. Shimomura,[28,50] T. Shioya,[71] K. Shoji,[61] P. Shukla,[4] A. Sickles,[7,25] C. L. Silva,[39] D. Silvermyr,[40,56] B. K. Singh,[3] C. P. Singh,[3,*] V. Singh,[3] M. Skolnik,[47] M. Slunečka,[9] K. L. Smith,[18,39] M. Snowball,[39] S. Solano,[47] R. A. Soltz,[38] W. E. Sondheim,[39] S. P. Sorensen,[69] I. V. Sourikova,[7] P. W. Stankus,[56] P. Steinberg,[7] E. Stenlund,[40] M. Stepanov,[43,*] A. Ster,[75] S. P. Stoll,[7] M. R. Stone,[12] T. Sugitate,[21] A. Sukhanov,[7] T. Sumita,[61] J. Sun,[67] Z. Sun,[15,23,67] J. Sziklai,[75] A. Takahara,[11] A. Taketani,[61,62] Y. Tanaka,[49]

K. Tanida,[29,62,65] M. J. Tannenbaum,[7] S. Tarafdar,[3,73,74] A. Taranenko,[51,66] G. Tarnai,[15] E. Tennant,[53] R. Tieulent,[19,41] A. Timilsina,[28] T. Todoroki,[61,62,71] M. Tomášek,[14,27] H. Torii,[11] C. L. Towell,[1] R. S. Towell,[1] I. Tserruya,[74] Y. Ueda,[21] B. Ujvari,[15,23] H. W. van Hecke,[39] M. Vargyas,[16,75] E. Vazquez-Zambrano,[13] A. Veicht,[13] J. Velkovska,[73] M. Virius,[14] V. Vrba,[14,27] N. Vukman,[77] E. Vznuzdaev,[59] R. Vértesi,[75] X. R. Wang,[53,62] D. Watanabe,[21] K. Watanabe,[61,63] Y. Watanabe,[61,62] Y. S. Watanabe,[11,32] F. Wei,[53] S. Whitaker,[28] S. Wolin,[25] C. L. Woody,[7] M. Wysocki,[56] B. Xia,[55] L. Xue,[19] C. Xu,[53] Q. Xu,[73] S. Yalcin,[67] Y. L. Yamaguchi,[11,67] H. Yamamoto,[71] A. Yanovich,[24] S. Yokkaichi,[61,62] I. Yoon,[65] J. H. Yoo,[33] I. Younus,[37,52] Z. You,[39] I. E. Yushmanov,[34] H. Yu,[53,58] W. A. Zajc,[13] A. Zelenski,[6] S. Zhou,[10] and L. Zou[8]

(PHENIX Collaboration)

[1]*Abilene Christian University, Abilene, Texas 79699, USA*
[2]*Department of Physics, Augustana University, Sioux Falls, South Dakota 57197, USA*
[3]*Department of Physics, Banaras Hindu University, Varanasi 221005, India*
[4]*Bhabha Atomic Research Centre, Bombay 400 085, India*
[5]*Baruch College, City University of New York, New York, New York, 10010 USA*
[6]*Collider-Accelerator Department, Brookhaven National Laboratory, Upton, New York 11973-5000, USA*
[7]*Physics Department, Brookhaven National Laboratory, Upton, New York 11973-5000, USA*
[8]*University of California-Riverside, Riverside, California 92521, USA*
[9]*Charles University, Faculty of Mathematics and Physics, 180 00 Troja, Prague, Czech Republic*
[10]*Science and Technology on Nuclear Data Laboratory, China Institute of Atomic Energy, Beijing 102413, People's Republic of China*
[11]*Center for Nuclear Study, Graduate School of Science, University of Tokyo, 7-3-1 Hongo, Bunkyo, Tokyo 113-0033, Japan*
[12]*University of Colorado, Boulder, Colorado 80309, USA*
[13]*Columbia University, New York, New York 10027, USA and Nevis Laboratories, Irvington, New York 10533, USA*
[14]*Czech Technical University, Zikova 4, 166 36 Prague 6, Czech Republic*
[15]*Debrecen University, H-4010 Debrecen, Egyetem tér 1, Hungary*
[16]*ELTE, Eötvös Loránd University, H-1117 Budapest, Pázmány P. s. 1/A, Hungary*
[17]*Ewha Womans University, Seoul 120-750, Korea*
[18]*Florida State University, Tallahassee, Florida 32306, USA*
[19]*Georgia State University, Atlanta, Georgia 30303, USA*
[20]*Hanyang University, Seoul 133-792, Korea*
[21]*Physics Program and International Institute for Sustainability with Knotted Chiral Meta Matter (WPI-SKCM^2), Hiroshima University, Higashi-Hiroshima, Hiroshima 739-8526, Japan*
[22]*Department of Physics and Astronomy, Howard University, Washington, DC 20059, USA*
[23]*HUN-REN ATOMKI, H-4026 Debrecen, Bem tér 18/c, Hungary*
[24]*IHEP Protvino, State Research Center of Russian Federation, Institute for High Energy Physics, Protvino, 142281, Russia*
[25]*University of Illinois at Urbana-Champaign, Urbana, Illinois 61801, USA*
[26]*Institute for Nuclear Research of the Russian Academy of Sciences, Prospekt 60-letiya Oktyabrya 7a, Moscow 117312, Russia*
[27]*Institute of Physics, Academy of Sciences of the Czech Republic, Na Slovance 2, 182 21 Prague 8, Czech Republic*
[28]*Iowa State University, Ames, Iowa 50011, USA*
[29]*Advanced Science Research Center, Japan Atomic Energy Agency, 2-4 Shirakata Shirane, Tokai-mura, Naka-gun, Ibaraki-ken 319-1195, Japan*
[30]*Jeonbuk National University, Jeonju, 54896, Korea*
[31]*Helsinki Institute of Physics and University of Jyväskylä, P.O. Box 35, FI-40014 Jyväskylä, Finland*
[32]*KEK, High Energy Accelerator Research Organization, Tsukuba, Ibaraki 305-0801, Japan*
[33]*Korea University, Seoul 02841, Korea*
[34]*National Research Center "Kurchatov Institute," Moscow, 123098 Russia*
[35]*Kyoto University, Kyoto 606-8502, Japan*
[36]*Laboratoire Leprince-Ringuet, Ecole Polytechnique, CNRS-IN2P3, Route de Saclay, F-91128, Palaiseau, France*
[37]*Physics Department, Lahore University of Management Sciences, Lahore 54792, Pakistan*
[38]*Lawrence Livermore National Laboratory, Livermore, California 94550, USA*
[39]*Los Alamos National Laboratory, Los Alamos, New Mexico 87545, USA*
[40]*Department of Physics, Lund University, Box 118, SE-221 00 Lund, Sweden*
[41]*IPNL, CNRS/IN2P3, Université Lyon 1, F-69622, Villeurbanne, France*
[42]*University of Maryland, College Park, Maryland 20742, USA*
[43]*Department of Physics, University of Massachusetts, Amherst, Massachusetts 01003-9337, USA*
[44]*MATE, Laboratory of Femtoscopy, Károly Róbert Campus, H-3200 Gyöngyös, Mátraiút 36, Hungary*
[45]*Department of Physics, University of Michigan, Ann Arbor, Michigan 48109-1040, USA*
[46]*Mississippi State University, Mississippi State, Mississippi 39762, USA*

[47]*Muhlenberg College, Allentown, Pennsylvania 18104-5586, USA*
[48]*Myongji University, Yongin, Kyonggido 449-728, Korea*
[49]*Nagasaki Institute of Applied Science, Nagasaki-shi, Nagasaki 851-0193, Japan*
[50]*Nara Women's University, Kita-uoya Nishi-machi Nara 630-8506, Japan*
[51]*National Research Nuclear University, MEPhI, Moscow Engineering Physics Institute, Moscow, 115409, Russia*
[52]*University of New Mexico, Albuquerque, New Mexico 87131, USA*
[53]*New Mexico State University, Las Cruces, New Mexico 88003, USA*
[54]*Physics and Astronomy Department, University of North Carolina at Greensboro, Greensboro, North Carolina 27412, USA*
[55]*Department of Physics and Astronomy, Ohio University, Athens, Ohio 45701, USA*
[56]*Oak Ridge National Laboratory, Oak Ridge, Tennessee 37831, USA*
[57]*IPN-Orsay, Univ. Paris-Sud, CNRS/IN2P3, Université Paris-Saclay, BP1, F-91406, Orsay, France*
[58]*Peking University, Beijing 100871, People's Republic of China*
[59]*PNPI, Petersburg Nuclear Physics Institute, Gatchina, Leningrad region, 188300, Russia*
[60]*Pusan National University, Pusan 46241, Korea*
[61]*RIKEN Nishina Center for Accelerator-Based Science, Wako, Saitama 351-0198, Japan*
[62]*RIKEN BNL Research Center, Brookhaven National Laboratory, Upton, New York 11973-5000, USA*
[63]*Physics Department, Rikkyo University, 3-34-1 Nishi-Ikebukuro, Toshima, Tokyo 171-8501, Japan*
[64]*Saint Petersburg State Polytechnic University, St. Petersburg, 195251 Russia*
[65]*Department of Physics and Astronomy, Seoul National University, Seoul 151-742, Korea*
[66]*Chemistry Department, Stony Brook University, SUNY, Stony Brook, New York 11794-3400, USA*
[67]*Department of Physics and Astronomy, Stony Brook University, SUNY, Stony Brook, New York 11794-3800, USA*
[68]*Sungkyunkwan University, Suwon, 440-746, Korea*
[69]*University of Tennessee, Knoxville, Tennessee 37996, USA*
[70]*Department of Physics, Tokyo Institute of Technology, Oh-okayama, Meguro, Tokyo 152-8551, Japan*
[71]*Tomonaga Center for the History of the Universe, University of Tsukuba, Tsukuba, Ibaraki 305, Japan*
[72]*United States Merchant Marine Academy, Kings Point, New York 11024, USA*
[73]*Vanderbilt University, Nashville, Tennessee 37235, USA*
[74]*Weizmann Institute, Rehovot 76100, Israel*
[75]*Institute for Particle and Nuclear Physics, HUN-REN Wigner Research Centre for Physics, (HUN-REN Wigner RCP, RMI) H-1525 Budapest 114, POBox 49, Budapest, Hungary*
[76]*Yonsei University, IPAP, Seoul 120-749, Korea*
[77]*Department of Physics, Faculty of Science, University of Zagreb, Bijenička c. 32 HR-10002 Zagreb, Croatia*
[78]*Department of Physics, School of Natural Sciences, University of Zambia, Great East Road Campus, Box 32379, Lusaka, Zambia*

(Received 22 August 2024; accepted 18 April 2025; published 24 June 2025; corrected 10 July 2025)

The jet cross section and jet-substructure observables in $p+p$ collisions at $\sqrt{s} = 200$ GeV were measured by the PHENIX Collaboration at the Relativistic Heavy Ion Collider (RHIC). Jets are reconstructed from charged-particle tracks and electromagnetic-calorimeter clusters using the anti-k_t algorithm with a jet radius of $R = 0.3$ for jets with transverse momentum within $8.0 < p_T < 40.0$ GeV/c and pseudorapidity $|\eta| < 0.15$. Measurements include the jet cross section, as well as distributions of SoftDrop-groomed momentum fraction (z_g), charged-particle transverse momentum with respect to jet axis (j_T), and radial distributions of charged particles within jets (r). Also measured was the distribution of $\xi = -\ln(z)$, where z is the fraction of the jet momentum carried by the charged particle. The measurements are compared to theoretical next-to and next-to-next-to-leading-order calculations, the PYTHIA and Herwig event generators, and to other existing experimental results. Indicated from these measurements is a lower particle multiplicity in jets at RHIC energies when compared to models. Also noted are implications for future jet measurements with sPHENIX at RHIC as well as at the future Electron-Ion Collider.

DOI: 10.1103/hpm9-qfp6

[*]Deceased.
[†]Contact author: akiba@rcf.rhic.bnl.gov

I. INTRODUCTION

Jets, the collimated sprays of particles originating from hard parton scatterings, were initially conceptualized as a probe of quantum chromodynamics (QCD) [1]. Perturbative QCD (pQCD) is broadly in good agreement with measurements of jets produced in high-energy collisions, particularly at high momentum and large radii [2]. At lower momenta [3] and small radii [4], it is necessary to include a good description of the nonperturbative contributions to jet production, including hadronization. Jet spectra at low momenta are also sensitive to the underlying event and effects such as color reconnections [3,5,6]. Measurements at lower momenta are important to test models for these nonperturbative components and their effect on jet production.

The use of jets has been expanded to include measurements of jet substructure, with a wide variety of observables sensitive to distribution of energy within the jet [2]. These observables are sensitive to final-state radiation patterns in QCD. At the Large Hadron Collider (LHC), where studies are dominated by high energy jets, pQCD and models generally reproduce data within $\approx 20\%$ for most substructure measurements [3,7–11]. Calculations of some observables at the Relativistic Heavy Ion Collider (RHIC) are likewise within $\approx 20\%$ of the data [12]. However, in lower-energy collisions, experimental and theoretical uncertainties have generally been large [13], and there are some measurements where theoretical calculations barely agree with the data within large uncertainties [14]. Monte Carlo generators and pQCD calculations are often used to predict the behavior of jets for proposed detectors, to determine corrections to measurements, and as a baseline for systems where jets may be modified, such as high-energy heavy ion collisions. Simultaneous comparisons between models and data for both cross sections and substructure can place substantial constraints on Monte Carlo models.

At the future Electron-Ion Collider (EIC) [15], jets will also serve as a tool to study the momentum space structure of hadrons as well as parton energy loss in cold nuclear matter [16]. Because the EIC will operate at a relatively low center-of-mass energy, closer to RHIC than the LHC, it is important to have measurements in $p+p$ collisions at comparable energies to test universality and factorization breaking effects [17].

Here are presented measurements of the jet cross section and several jet substructure measurements in $p+p$ collisions at $\sqrt{s} = 200$ GeV. The technique is first summarized, including details of the unfolding and the simulations used for detector corrections. The results are then presented and compared to pQCD calculations and output from the PYTHIA and Herwig event generators, and finally, the implications of these results are discussed.

II. JET RECONSTRUCTION AND UNFOLDING

A. PHENIX detector and dataset

Combined $p+p$ datasets collected during 2012 and 2015 were used in this analysis. The 2012 dataset sampled an integrated luminosity of 1.55 pb^{-1} using an electromagnetic-calorimeter trigger, while the 2015 dataset sampled 13.5 pb^{-1} using a similar trigger with a higher-energy threshold.

Jets were measured in the PHENIX central arms [18]. Each arm covers a pseudorapidity range of $|\eta| < 0.35$ and an azimuthal range of $\pi/2$. Charged-particle tracks were measured by a set of multiwire proportional chambers, including an inner drift chamber and multiple outer pad chambers. Energy deposits from neutral particles are measured by the finely segmented electromagnetic calorimeter (EMCal), consisting of lead-scintillator modules in the west arm, and lead-scintillator and lead-glass Čerenkov modules in the east arm. The modules have a resolution determined by beam tests [19,20] to be $\delta E/E = 8.1\%/\sqrt{E} \oplus 2.1\%$ and $5.9\%/\sqrt{E} \oplus 0.8\%$, respectively, where E is in GeV, and were calibrated through the reconstruction of neutral pion decays. The calorimeter further provides a trigger signal initiated by the presence of at least 1.6 GeV (2012) or 2.1 GeV (2015) of energy deposited in one of the groups of overlapping 4×4 towers in the lead-glass or lead-scintillator modules, respectively. To reduce the inefficiencies introduced by dead areas in the outer pad chambers, a confirming hit with an energy greater than a minimum-ionizing particle is required in the EMCal if a drift chamber track does not have a confirming hit in the outer pad chamber. In addition to the spectrometer arms, a pair of beam-beam counter (BBC) detectors situated along the beam line at $3.0 < |\eta| < 3.9$ provide the minimum-bias (MB) trigger signal and reconstruct the z position of the primary vertex. The BBCs measure charged particles and are used to determine the collision time and vertex position along the beam axis.

B. Jet reconstruction

Jets were reconstructed using the anti-k_t algorithm [21,22] with radius parameter $R = 0.3$ from electromagnetic clusters in the EMCal [23] and charged-particle tracks (in the drift and pad chambers) [24] each with a minimum p_T of 0.5 GeV/c. The anti-k_t algorithm, the de facto standard for hadronic collisions, was chosen because it clusters outward from the hard core of jets, thus reducing the sensitivity to detector edges. A set of criteria designed to select charged particles with a well-measured momentum, and reject conversions and ghost tracks was applied to candidate reconstructed tracks. Clusters consistent with arising from the same particle as a reconstructed track were rejected to avoid double counting the jet constituent energy. To eliminate both beam and detector backgrounds, jets were required to have at least three constituents, have a charged fraction of momentum between 0.3 and 0.7, be within $|\eta_{\rm jet}| < 0.15$, and be reconstructed in the same PHENIX detector arm that provided the trigger signal. Only events passing the offline-event vertex cut $|z_{\rm vertex}| < 10$ cm were accepted. Jets were required to be fully contained within the η, ϕ acceptance of the PHENIX arm, where the η acceptance takes into account the longitudinal vertex location. The reconstructed jets average between 45% and 55% of the true jet energy, with the average fraction increasing slowly with jet p_T. A jet at a reconstructed p_T of 10 GeV/c has a mean of 4.5 track and cluster constituents. This rises to a mean of six track and cluster constituents at a reconstructed p_T of 20 GeV/c. In addition to the jet cross section, the following substructure properties were also measured:

(1) distributions of SoftDrop [25,26] groomed momentum fraction (z_g),
(2) charged-particle transverse momentum with respect to the jet axis (j_T),
(3) radial distributions of charged particles within the jet ($r = \sqrt{\Delta\phi^2 + \Delta\eta^2}$), where $\Delta\phi$ and $\Delta\eta$ are the distances from a charged particle to the jet axis in azimuthal angle and pseudorapidity respectively, and
(4) distributions of $\xi = -\ln(z)$, where z is the fraction of the jet momentum carried by the charged particle.

C. Unfolding

The reconstructed jet distributions were corrected for the detector response by Bayesian unfolding [27] using the "RooUnfold" framework [28]. The response matrix for unfolding was obtained using a simulation of $p+p$ collision events with the PHENIX detector response simulated by Geant3 [29]. In the first step, PYTHIA6 [30] Tune A was used with QCD hard-scattering processes selected, along with an additional Gaussian partonic k_t smearing with a width of 3 GeV as this combination better reproduces two-particle correlations previously measured in PHENIX [31]. To sample the full jet cross section as a function of jet p_T with adequate statistics, the PYTHIA6 events were generated in fixed ranges of partonic p_T. The full event sample was obtained by recombination using the cross section reported by PYTHIA6. The PHENIX simulations included run-specific detector configurations, including tracking and EMCal tower inefficiency and trigger efficiency maps. The simulation response was matched to the reconstructed data, and the same kinematic and selection cuts used in the data were applied to the reconstructed results in the simulation. A total of $\approx 832,000$ PYTHIA6 events per run configuration were processed through the full Geant-based simulation of the PHENIX detector.

In processing the simulated events to generate the response matrix, jet finding is performed with both the truth simulation input and the reconstructed output of the simulations. Truth jets are determined directly from the MC-generator output, excluding neutrinos. The same binning was used for both the truth input and reconstructed output, both in jet p_T and in the substructure distribution variables. When constructing a response matrix three possibilities need to be considered:

(1) A matched reconstructed and truth jet pair is found. This is used to define the mapping between the reconstructed and truth p_T and substructure quantities.
(2) A corresponding reconstructed jet is not found for a given truth jet. This jet may not have been found due to detector inefficiencies or acceptance limitations, analysis cuts, or failed to satisfy a trigger condition. This inefficiency must be accounted for when reconstructing the truth p_T spectrum and substructure distributions.
(3) A reconstructed jet is found that does not match a truth jet in the simulated data. This is a fake jet and typically represents a contribution from the underlying event. This contribution is more important at low jet p_T, and the contribution of these jets are subtracted from the measured jet p_T spectrum and substructure distributions as part of the unfolding process.

Response matrices are defined for the cross section, which are used for one-dimensional unfolding in jet p_T. For the substructure distributions, two-dimensional unfolding is performed in both jet p_T and the substructure variable. This is a commonly used method which takes advantage of a relatively large statistical sample of simulated data to extract information from measurements that have a substantial smearing in the reconstructed quantities. An example of the unfolding matrix for the two-dimensional unfolding for the ξ substructure variable is shown in Fig. 1.

To test the unfolding procedure a closure test was performed. Two statistically independent samples of PYTHIA6 simulated events were used to determine the response matrices and provide a sample that was treated as pseudodata. The pseudodata were unfolded following the exact same procedures as for data, and the results compared to the PYTHIA6 truth distributions. The results of the closure test indicate that the unfolding method can reproduce the input distribution with a high degree of fidelity, and there are no errors in the procedure that cause a deviation between the input and unfolded distributions. Tests with Bayesian and singular value decomposition unfolding using PYTHIA6 pseudodata and reweighting the cross section to next-to-leading-order (NLO) predictions showed that the unfolding converged after two iterations. In what follows Bayesian unfolding is used with two iterations, and the difference between the second and third iteration is used as a systematic uncertainty.

An examination of the unfolding using the initial PYTHIA6 sample showed that the integrals of the $\xi = -\ln(z)$, j_T and r distributions, which is the average number of charged

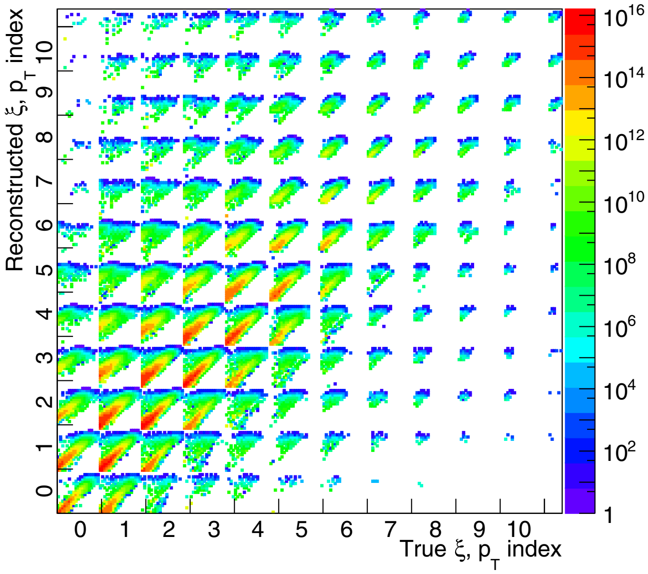

FIG. 1. An example of the unfolding matrix for a two-dimensional unfolding of the ξ distribution. The matrix is viewed as a set of one-dimensional unfolding matrices in jet p_T, shown as a two-dimensional plot in reconstructed vs true jet p_T, as a function of the bin in the variable ξ.

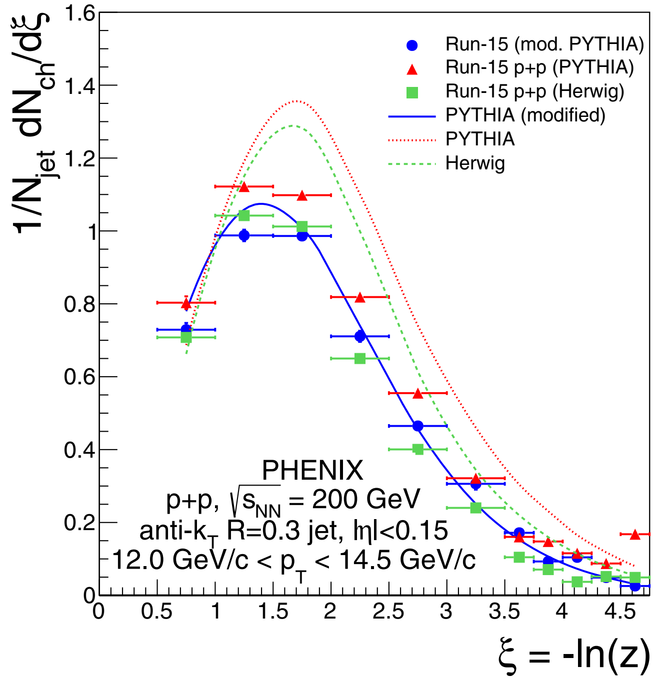

FIG. 2. Unfolded ξ distributions (data points) obtained using Herwig, PYTHIA and modified PYTHIA6 compared to the 2015 dataset results unfolded using the different MC models (dashed lines). Both PYTHIA6 and PYTHIA8 produce compatible results and are shown by one curve in the figure. The standard versions of PYTHIA6 and 8 overestimate the number of jet constituents and systematically pull the unfolded distributions to higher values, as does the Herwig model. The modified version of PYTHIA6, described in the text, shows a good agreement between the unfolded and model distributions and is used for subsequent results in this paper.

particles in the jet, were consistent with each other but lower than the PYTHIA6 input by approximately one charged particle per jet, with a weak dependence on jet p_T. Similar results were obtained using the PYTHIA8 [32] event generator in its standard configuration with the Monash tune [33]. A similar discrepancy between measurements and PYTHIA6 was observed at RHIC in inclusive $\pi^{\pm}$ yields [34]. This difference leads to a bias in the unfolded substructure distributions, as well as a systematic uncertainty in the determination of the efficiencies used to correct the jet p_T cross section. As described below, to mitigate this bias the choice is made to modify the PYTHIA6 events used to generate the unfolding matrices in an iterative fashion until the PYTHIA6 events better matched the unfolded substructure distributions.

As an example, unfolded ξ distributions obtained using different versions of PYTHIA and Herwig are shown in Fig. 2. The Herwig and unmodified PYTHIA references tend to pull the unfolded distributions systematically high, while iteratively adjusting the MC input to be closer to the data allows the input distribution to converge to the unfolded data.

Upon examining the difference between the initial unfolding with PYTHIA6 for the charged-particle substructure distributions, it was noted that the difference in r between the unfolded data and the PYTHIA6 model was predominantly at large distances from the jet axis, which is correlated with a deficit in the unfolded data at large j_T. This indicates that a simple model that reduces the number of particles, based on the observed radial distribution in the data, could simultaneously improve the model agreement with multiple unfolded substructure distributions. Given these observations, the choice was made to modify the PYTHIA output to produce a reference that better matches the unfolded data:

(1) Final-state particles are clustered using the FastJet [22] anti-k_t algorithm with jet radius $R = 0.3$.
(2) The ratio of the unfolded data to PYTHIA6 in the r distributions for each jet p_T bin is used to randomly remove constituent particles from the jet. This removal is applied equally to charged and neutral particles. The transverse momentum of the removed particles is recorded.
(3) To avoid changing the overall shape of the jet cross section as a function of jet p_T, the momentum of the remaining constituents is rescaled to account for the particles that were removed from the jet.

Each step in this process required the generation and simulation of complete PYTHIA6 event samples as described above. It was found that the agreement between the integral of the ξ, j_T and r distributions was in good agreement after two iterations. This event sample is referred to as "modified PYTHIA6," and the final results in what follows were generated by unfolding using the modified PYTHIA6 event

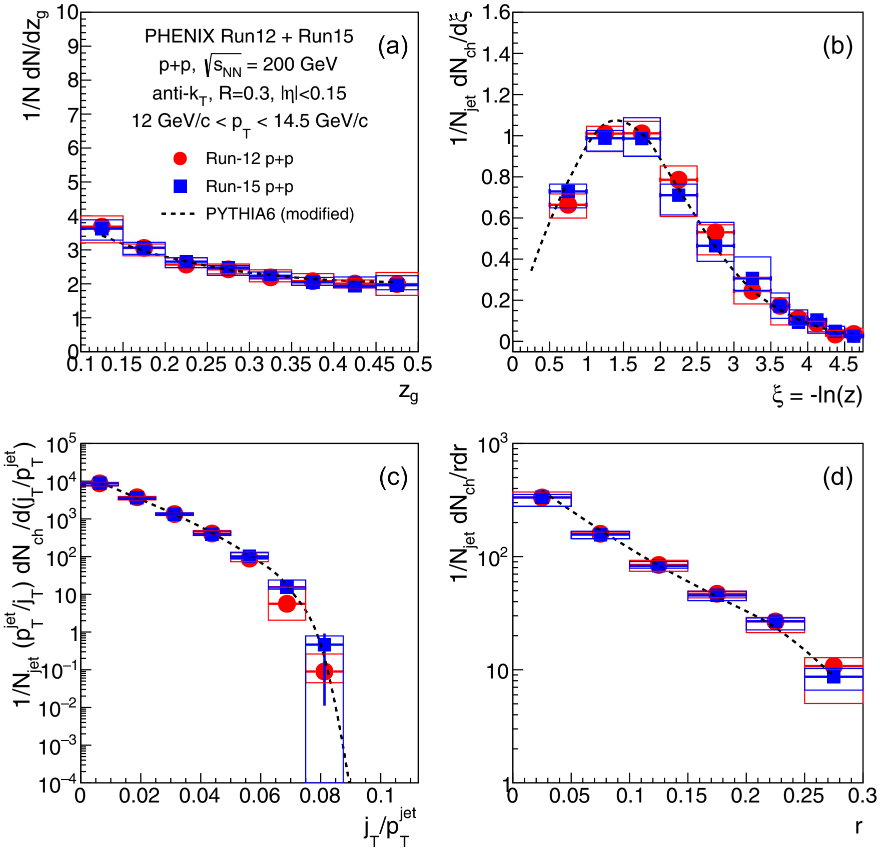

FIG. 3. Comparison of Run12 and Run15 results for four unfolded substructure distributions obtained using modified PYTHIA6 unfolding matrices. The boxes show the systematic uncertainties on the unfolded data points, exclusive of the model systematic described in the text.

sample. The z_g distribution is relatively insensitive to the PYTHIA6 model used in the unfolding, as expected by its construction. Note that although the PYTHIA output was modified using the radial distribution of particles in the jet, the procedure also improves the agreement for the ξ and j_T/p_T^{jet} distributions as well. The approach chosen to modify PYTHIA6 by reducing the number of constituents and rescaling their momentum to keep the jet momentum unchanged produces a harder fragmentation spectrum preferred by the data, as can be seen in Fig. 2.

The consistency of the substructure distributions extracted separately from the 2012 and 2015 data and unfolded using the modified PYTHIA6 reference is shown in Fig. 3. The final results are produced by combining the 2012 and 2015 distributions using the full correlation matrix extracted from the separate unfoldings to produce the final combined result.

D. Systematic uncertainties

Systematic uncertainties were calculated for each run period by comparing variations of cuts, efficiencies, and the unfolding procedure to the baseline. These variations included the following:

(1) The Bayesian regulation parameter in the unfolding was varied from the nominal two to three iterations.
(2) The charged fraction cut on jets was tightened to 0.3–0.6 (from 0.3 to 0.7), and the number of constituents (nc) cut was raised from $nc \geq 3$ to $nc \geq 5$.
(3) The outermost pad chamber or EMCal cluster matching cut for drift chamber tracks was lowered to 1.5σ (from 3σ). This is our dominant source of tracking inefficiency.
(4) The minimum p_T of tracks used for jet finding was raised to 1.5 GeV/c, keeping the cluster energy cut at 0.5 GeV/c.
(5) The minimum energy of clusters used for jet finding was raised to 1.5 GeV, keeping the track p_T cut at 0.5 GeV/c.
(6) The energy of EMCal clusters is varied up and down by the scale uncertainty of $\pm 3\%$, as determined by measurements of π^0 mesons.
(7) The p_T of charged tracks is varied up and down by $\pm 2\%$, consistent with the estimated track momentum scale uncertainty in PHENIX.
(8) The overall trigger efficiency was varied within uncertainties.

(9) The difference between a separate reconstruction of the east and west detector arm results is also added in quadrature to the systematic uncertainty, although this difference was negligible.

To determine systematic uncertainties, the variations in cuts are applied to both the data and the modified PYTHIA-MC generator processed through the Geant-based PHENIX simulation. New unfolding matrices are generated, the data are unfolded again, and the results are compared with the baseline. For energy- and momentum-scale errors, the energy scale in the data is shifted, and the results are unfolded with the standard unfolding matrix. At low jet p_T different sources of systematic uncertainty are comparable, while at highest p_T the uncertainties related to the unfolding procedure dominate. For each run period the systematics determined in this fashion are assumed to be uncorrelated and are combined in quadrature. An additional overall 10% systematic uncertainty is applied to the cross section measurement based on the uncertainty in the cross section measured by the BBC.

The systematic uncertainties for the combined result are produced by combining the 2012 and 2015 systematic uncertainties using the full correlation matrix extracted from the separate unfoldings, assuming that the systematic uncertainties are correlated through the unfolding in the same way as the statistical uncertainties.

Finally, a systematic uncertainty based on the model dependence of the unfolding procedure is applied by comparing the results unfolded using PYTHIA8 and Herwig to the results unfolded using modified PYTHIA6. A point-by-point-modeling systematic uncertainty is combined in quadrature with the systematic uncertainties described above to produce the final systematic uncertainty on each point in the cross section and substructure distribution measurements. The modeling systematic uncertainty is subdominant for all but the two highest jet p_T points in the cross section measurements. However, the modeling systematic uncertainty dominates for most points in the substructure distributions, depending on the specific distribution and jet p_T bin.

III. RESULTS

A. Jet cross section

The jet cross section is calculated as

$$\frac{d^2\sigma}{dp_T d\eta} = \frac{\sigma_{\mathrm{BBC}}}{c_{\mathrm{BBC}}^{hard} N_{\mathrm{MB}}} \frac{N_{\mathrm{jet}}(p_T)}{\Delta p_T \Delta\eta}, \quad (1)$$

where $\sigma_{\mathrm{BBC}} = 23.0 \pm 2.2$ mb is the MB cross section sampled by the BBC; $c_{\mathrm{BBC}}^{\mathrm{hard}} = 0.79 \pm 0.02$ is the correction factor to account for the BBC sampling a larger fraction of the cross section when the collision includes a hard scattering process. N_{MB} is the effective number of MB events sampled by the trigger that pass event-level cuts in offline analysis ($|z_{\mathrm{vertex}}| < 10$ cm).

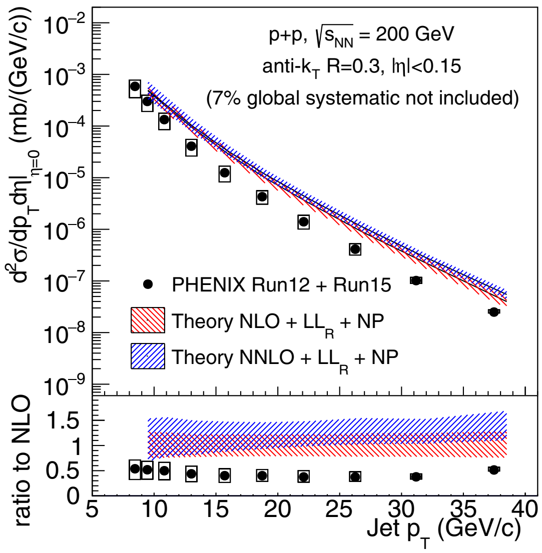

FIG. 4. The jet differential cross section as a function of jet p_T. Statistical uncertainties are typically smaller than the data points while systematic uncertainties are shown with boxes. An overall normalization systematic of 7% is not included in the point-by-point systematic uncertainties. The bottom panel shows the ratio of the data and NNLO calculations to the NLO calculations. The theory bands are explained in the text and were obtained by matching the NLO and NNLO predictions including matching to leading-logarithmic resummation (LL_R) in the jet radius and nonperturbative corrections (NP).

The jet differential cross section in $p + p$ collisions at $\sqrt{s} = 200$ GeV as a function of p_T is shown in Fig. 4. The bands in Fig. 4 show theoretical calculations obtained by matching the NLO [35,36] and NNLO predictions [37] to leading-logarithmic resummation of the jet radius [38]. The matching is done using the approach described in [39], adopting the partonic scalar sum as the central scale choice and using the seven-point rule for uncertainties (adding the large-angle and small-angle uncertainties in quadrature). The perturbative calculations are supplemented with nonperturbative (NP) corrections extracted from Monte Carlo simulations, as discussed also in [39]. These corrections are obtained as the average and envelope of five setups: PYTHIA8.306 with tune 4C [40], PYTHIA8.306 with tune Monash13 [33], PYTHIA8.306 with tune ATLAS14 [41] (with NNPDF2.3 [42]), Sherpa2.2.11 [43] (default tune), and Herwig7.2.0 [44] (default tune). The nonperturbative corrections include hadronization and multiparton interactions, and their uncertainties are added in quadrature to the perturbative scale uncertainties.

Figure 4 shows that theory substantially overestimates the measured cross sections. This observation is consistent within systematic uncertainties with a previously published comparison between jets measured by the STAR Collaboration at RHIC energies using a midpoint-cone algorithm and NLO calculations without leading-logarithm resummation [13], as well as results from the ALICE Collaboration for the low-p_T jet cross section at a higher center-of-mass energy [45] when compared to MC generators. However, the ALICE results show a jet p_T dependence while the PHENIX ratio is flat as a function of jet p_T. Studies of the jet cross section relative to NLO predictions at LHC energies indicate that NLO predictions overestimate the jet cross section at small anti-k_t R, while the agreement is better at larger values of R [46]. This could indicate that the angular distribution of particles in the jet is not accurately reproduced by NLO calculations. As noted above, NLO calculations work at the partonic level, and use a hadronization model to make a comparison to the experimental data measured at the hadron level. The hadronization correction effectively shifts partonic jet p_T distributions to lower hadronic jet p_T. As shown in Ref. [39], the p_T shift of the partonic jet due to the hadronization correction is larger at jet momenta lower than LHC energies, and there is a substantial variation between Monte Carlo models. The hadronization correction could also be substantially affected if the fragmentation of the jet is substantially different in data than in the Monte Carlo models, as indicated by the unfolding of the PHENIX data. This could lead to an underprediction of the p_T shift by the hadronization and an overprediction of the theory cross section compared to data.

B. Jet substructure distributions

The z_g distribution is calculated using all jet constituents, while the distributions in ξ, j_T and r are calculated for charged particles only. To derive z_g from a previously determined $R = 0.3$ anti-k_t jet, the jet constituents are reclustered using the Cambridge-Aachen algorithm [47]. This algorithm works by clustering from small angles to larger angles, and the clustering tree can be accessed to determine the last two subclusters that were combined to determine the final jet. The quantity $z_g = \frac{\min(p_{T1}, p_{T2})}{p_{T1}+p_{T2}}$, where p_{T1} and p_{T2} are subcluster transverse momenta, is evaluated, and if $z_g \leq 0.1$ the lowest p_T cluster is dropped and the remaining subjet is declustered and evaluated again. This continues until the condition $z_g > 0.1$ is met or the jet runs out of constituents. The SoftDrop z_g was first measured by the CMS Collaboration in $p+p$ and Pb + Pb collisions at $\sqrt{s} = 5.02$ TeV at the LHC for jets with $p_T > 140$ GeV/c [48], and later by the STAR Collaboration at RHIC energies [49,50]. Figure 5 shows the SoftDrop [25,26] groomed momentum fraction z_g, with SoftDrop condition $z_{\rm cut} = 0.1$ and SoftDrop $\beta = 0$ for different p_T bins and the STAR results [49] for different values of anti-k_t R. The STAR results are in good qualitative agreement with the PHENIX data. With increasing jet p_T the distributions get steeper, demonstrating that jets with highly asymmetric splittings are enhanced.

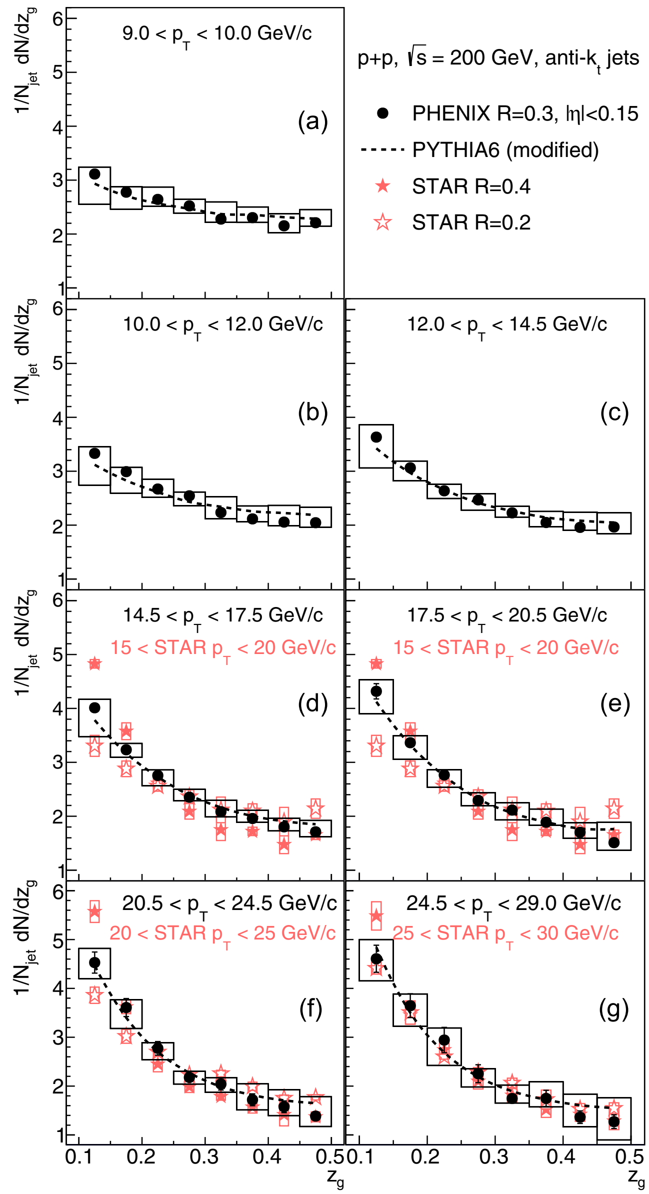

FIG. 5. Distribution of the SoftDrop groomed momentum fraction z_g for different jet p_T bins compared to the modified PYTHIA6 model used in the unfolding and STAR results from [49]. Standard SoftDrop parameters were used ($z_{\rm cut} < 0.1$ and $\beta = 0$).

Figure 6 shows the distribution of charged particles as a function of $\xi = -\ln(z)$, where z is the fraction of the jet momentum carried by the charged particle, for different p_T bins. This distribution is typically referred to as the fragmentation function. As the jet p_T increases, the observed ξ distributions shift right, or to smaller constituent momentum fractions z. This is highlighted in Fig. 6(g), which compares the lowest and highest jet momenta. The PHENIX measurements are limited to $\xi > 0.6$ by the jet-charged-momentum-fraction cut. A deficit of charged particles in the jet relative to the modified PYTHIA6 model grows as a function of jet p_T between $1 < \xi < 2.5$.

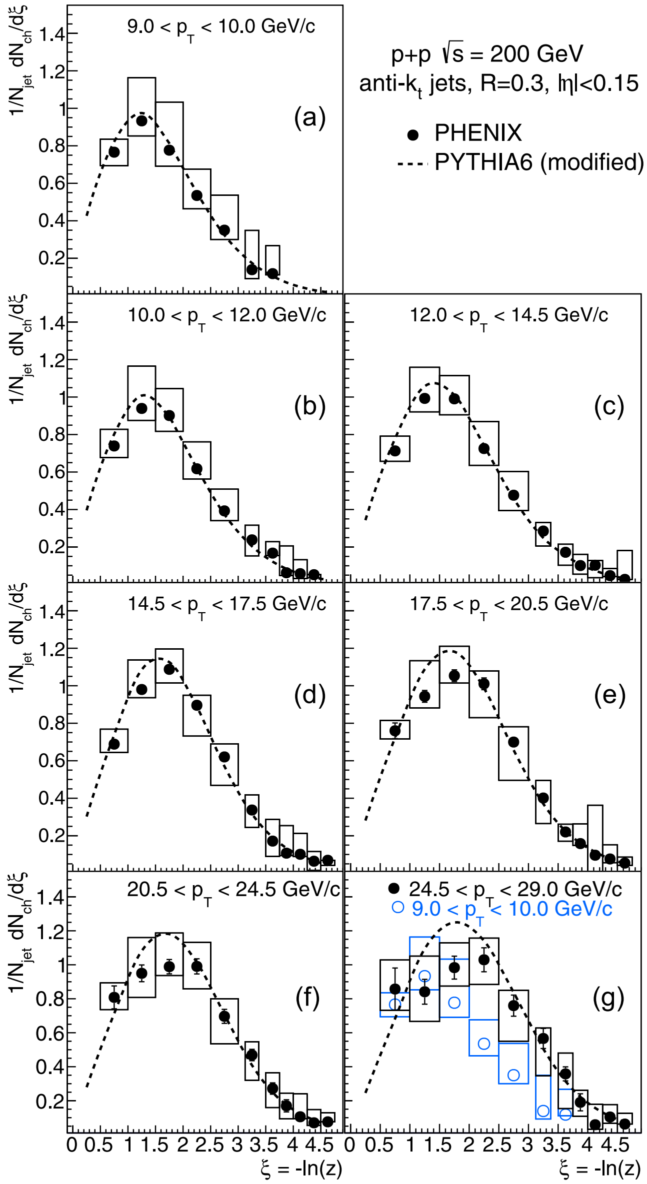

FIG. 6. ξ distributions for different jet p_T bins compared to the modified PYTHIA6 model used in the unfolding.

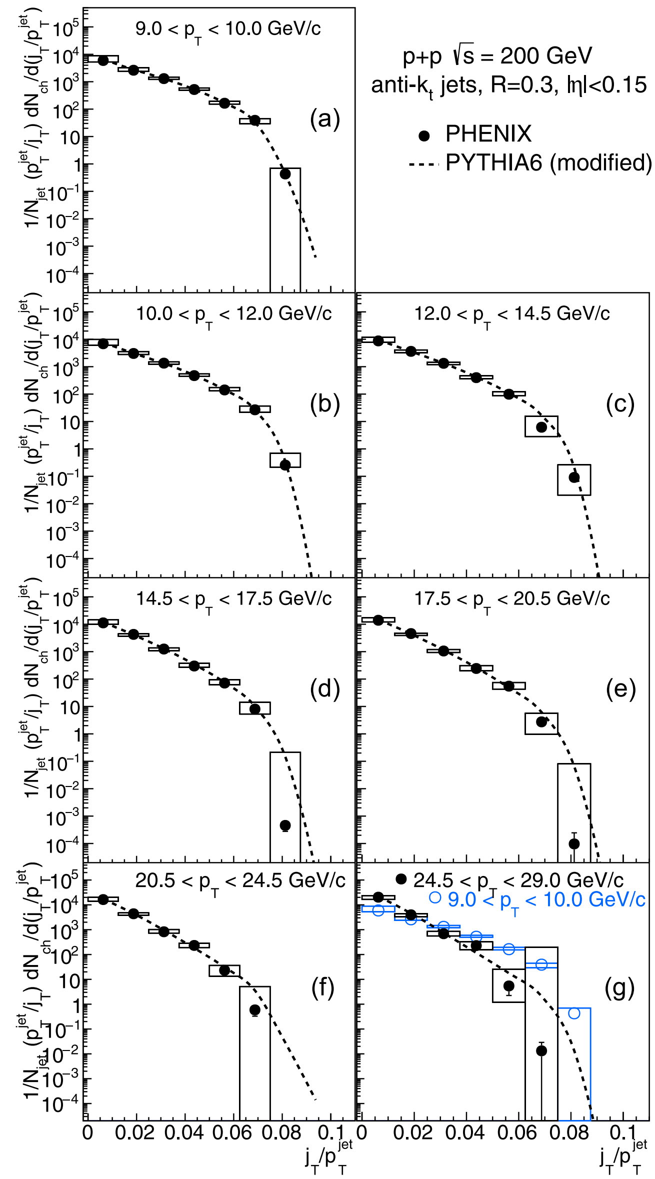

FIG. 7. The j_T/p_T^{jet} distributions for different jet p_T bins compared to the modified PYTHIA6 model used in the unfolding.

Figure 7 shows the distribution of the charged particle transverse momentum with respect to the jet axis j_T/p_T^{jet}, where p_T^{jet} is the jet transverse momentum, for different jet p_T bins. Figure 7(g), which compares the lowest and highest jet-momenta bins, indicates that j_T scales up with increasing jet p_T slower than the jet p_T itself. This is consistent with the changes observed in the r distribution.

The radial distribution of charged particles within the jet with respect to the jet axis (r) is shown in Fig. 8 as a function of jet p_T. The distribution of particles in the jet as a function of distance from the jet axis shows a significant increase at small r with increasing jet p_T, as can be seen in Fig. 8(g), where both the lowest and highest jet p_T bins are superimposed. This indicates the development of a higher particle density in the core of the jet with increasing jet p_T, which is consistent with the expected increase in the contribution of quark jets over gluon jets with increasing jet p_T at RHIC [34].

IV. SUMMARY AND CONCLUSIONS

In summary, presented here are the jet p_T-differential cross section and jet substructure distributions in $p + p$ collisions at $\sqrt{s} = 200$ GeV. Jets were reconstructed using the anti-k_t algorithm with a jet radius $R = 0.3$ for jets with transverse momentum within $8.0 < p_T < 40.0$ GeV$/c$ and pseudorapidity $|\eta| < 0.15$. The results were unfolded for experimental and detector effects. The unfolding indicates a lower average charged particle multiplicity is observed in

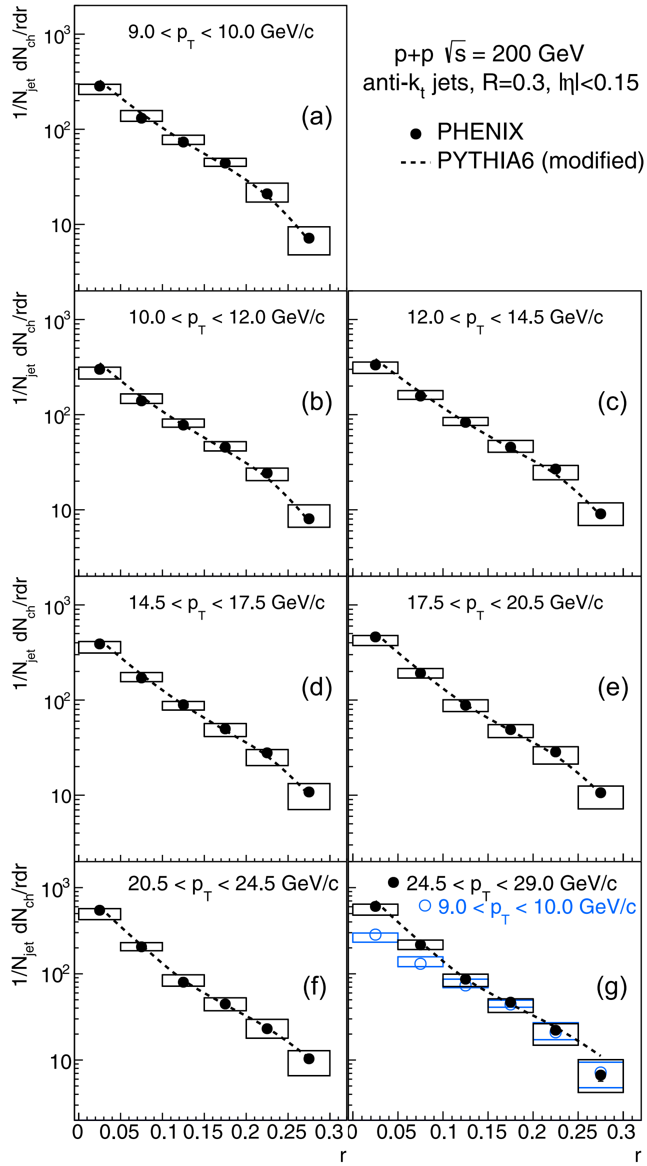

FIG. 8. r distributions for different jet p_T bins compared to the modified PYTHIA6 model used in the unfolding.

the PHENIX data than in the PYTHIA event generators, as much as one particle at the highest measured jet p_T.

These results indicate that NLO and NNLO predictions are higher than the measured jet cross section at RHIC, a result that is within the large systematic errors in a prior measurement [13]. This may indicate a limitation of the procedure used to translate from the partonic to the hadronic cross section, which requires Monte Carlo generators for the NP corrections. The measured data indicate a lower particle multiplicity at these center-of-mass energies and jet momenta than in the event generators used to calculate these corrections, while measurements at the LHC indicate that NLO calculations overestimate the jet cross section at small anti-k_t R. This indicates there may be multiple effects contributing to the disagreement between QCD calculations of the jet cross section and the measured data.

Presented were unfolded distributions in jets for $z_g, \xi, j_T/p_T^{\text{jet}}$, and r. The measured z_g distribution agrees well with the STAR results and becomes steeper with increasing jet p_T. The ξ distribution shifts toward a lower momentum fraction within the range measured in the PHENIX data. The j_T/p_T^{jet} distribution stays relatively unchanged with increasing jet p_T, while the r distribution shows a significant increase at small r with increasing jet p_T, consistent with an increasing fraction of quark jets at higher jet p_T.

In conclusion, these measurements contribute to an improved understanding of the jet cross section and substructure in $p + p$ collisions at RHIC, and are essential to be able to exploit new data from the sPHENIX detector, which will measure jets in heavy-ion collisions at RHIC with unprecedented precision [51]. In addition, as the center-of-mass energies and p_T range will be similar these results will also help inform jet measurements at the future Electron-Ion Collider.

ACKNOWLEDGMENTS

We thank the staff of the Collider-Accelerator and Physics Departments at Brookhaven National Laboratory and the staff of the other PHENIX participating institutions for their vital contributions. We acknowledge support from the Office of Nuclear Physics in the Office of Science of the Department of Energy, the National Science Foundation, Abilene Christian University Research Council, Research Foundation of SUNY, and Dean of the College of Arts and Sciences, Vanderbilt University (USA), Ministry of Education, Culture, Sports, Science, and Technology and the Japan Society for the Promotion of Science (Japan), Natural Science Foundation of China (People's Republic of China), Croatian Science Foundation and Ministry of Science and Education (Croatia), Ministry of Education, Youth and Sports (Czech Republic), Centre National de la Recherche Scientifique, Commissariat à l'Énergie Atomique, and Institut National de Physique Nucléaire et de Physique des Particules (France), J. Bolyai Research Scholarship, EFOP, the New National Excellence Program (ÚNKP), NKFIH, and OTKA (Hungary), Department of Atomic Energy and Department of Science and Technology (India), Israel Science Foundation (Israel), Basic Science Research and SRC (CENuM) Programs through NRF funded by the Ministry of Education and the Ministry of Science and ICT (Korea), Ministry of Education and Science, Russian Academy of Sciences, Federal Agency of Atomic Energy (Russia), VR and Wallenberg Foundation (Sweden), University of Zambia, the Government of the Republic of Zambia (Zambia), the U.S. Civilian Research and Development Foundation for the Independent States of the Former Soviet Union, the

Hungarian American Enterprise Scholarship Fund, the U.S.-Hungarian Fulbright Foundation, and the US-Israel Binational Science Foundation.

DATA AVAILABILITY

The data that support the findings of this article are not publicly available. The values in the plots associated with this article are stored in HEPData [52].

[1] G. F. Sterman and S. Weinberg, Jets from quantum chromodynamics, Phys. Rev. Lett. **39**, 1436 (1977).

[2] R. Kogler, B. Nachman, A. Schmidt, L. Asquith, E. Winkels, M. Campanelli, C. Delitzsch, P. Harris, A. Hinzmann, D. Kar, C. McLean, J. Pilot, Y. Takahashi, N. Tran *et al.*, Jet substructure at the Large Hadron Collider: Experimental review, Rev. Mod. Phys. **91**, 045003 (2019).

[3] S. Acharya *et al.* (ALICE Collaboration), Measurement of charged jet cross section in pp collisions at $\sqrt{s} = 5.02$ TeV, Phys. Rev. D **100**, 092004 (2019).

[4] B. Abelev *et al.* (ALICE Collaboration), Measurement of the inclusive differential jet cross section in pp collisions at $\sqrt{s} = 2.76$ TeV, Phys. Lett. B **722**, 262 (2013).

[5] F. Abe *et al.*, Evidence for color coherence in $p\bar{p}$ collisions at $\sqrt{s} = 1.8$ TeV, Phys. Rev. D **50**, 5562 (1994).

[6] F. Abbott *et al.*, Color coherent radiation in multijet events from collisions at $\sqrt{s} = 1.8$ TeV, Phys. Lett. B **414**, 419 (1997).

[7] S. Acharya *et al.* (ALICE Collaboration), Measurement of inclusive and leading subjet fragmentation in pp and Pb–Pb collisions at $\sqrt{s_{NN}} = 5.02$ TeV, J. High Energy Phys. 05 (2023) 245.

[8] S. Acharya *et al.* (ALICE Collaboration), Measurements of the groomed jet radius and momentum splitting fraction with the soft drop and dynamical grooming algorithms in pp collisions at $\sqrt{s} = 5.02$ TeV, J. High Energy Phys. 05 (2023) 244.

[9] S. Acharya *et al.* (ALICE Collaboration), Jet fragmentation transverse momentum distributions in pp and p-Pb collisions at $\sqrt{s}$, $\sqrt{s_{NN}} = 5.02$ TeV, J. High Energy Phys. 09 (2021) 211.

[10] S. Acharya *et al.* (ALICE Collaboration), Measurements of inclusive jet spectra in pp and central Pb-Pb collisions at $\sqrt{s_{\rm NN}} = 5.02$ TeV, Phys. Rev. C **101**, 034911 (2020).

[11] A. Tumasyan *et al.* (CMS Collaboration), Measurements of jet multiplicity and jet transverse momentum in multijet events in proton–proton collisions at $\sqrt{s} = 13$ TeV, Eur. Phys. J. C **83**, 742 (2023).

[12] J. Adam *et al.* (STAR Collaboration), Measurement of groomed jet substructure observables in $\mathrm{p+p}$ collisions at $\sqrt{s} = 200$ GeV with STAR, Phys. Lett. B **811**, 135846 (2020).

[13] B. I. Abelev *et al.* (STAR Collaboration), Longitudinal double-spin asymmetry and cross section for inclusive jet production in polarized proton collisions at $\sqrt{s} = 200$ GeV, Phys. Rev. Lett. **97**, 252001 (2006).

[14] M. Abdallah *et al.* (STAR Collaboration), Invariant jet mass measurements in pp collisions at $\sqrt{s} = 200$ GeV at RHIC, Phys. Rev. D **104**, 052007 (2021).

[15] F. Willeke and J. Beebe-Wang, Electron Ion Collider conceptual design report 2021, 10.2172/1765663 (2021).

[16] R. Abdul Khalek *et al.*, Science requirements and detector concepts for the Electron-Ion Collider, Nucl. Phys. **A1026**, 122447 (2022).

[17] T. C. Rogers and P. J. Mulders, No generalized TMD-factorization in hadro-production of high transverse momentum hadrons, Phys. Rev. D **81**, 094006 (2010).

[18] K. Adcox *et al.* (PHENIX Collaboration), PHENIX detector overview, Nucl. Instrum. Methods Phys. Res., Sect. A **499**, 469 (2003).

[19] G. David, Y. Goto, E. Kistenev, S. Stoll, S. White, C. Woody, A. Bazilevsky, S. Belikov, S. Chernichenkov, A. Denisov, V. Kochetkov, Y. Melnikov, V. Onuchin, V. Semenov, V. Shelikhov, A. Soldatov, and A. Usachev (PHENIX Collaboration), The PHENIX lead-scintillator electromagnetic calorimeter: Test beam and construction experience, IEEE Trans. Nucl. Sci. **45**, 692 (1998).

[20] L. Aphecetche *et al.* (PHENIX Collaboration), PHENIX calorimeter, Nucl. Instrum. Methods Phys. Res., Sect. A **499**, 521 (2003).

[21] M. Cacciari, G. P. Salam, and G. Soyez, The anti-k_t jet clustering algorithm, J. High Energy Phys. 04 (2008) 063.

[22] M. Cacciari, G. P. Salam, and G. Soyez, FastJet user manual, Eur. Phys. J. C **72**, 1896 (2012).

[23] J. Mitchell *et al.* (PHENIX Collaboration), Event reconstruction in the PHENIX central arm spectrometers, Nucl. Instrum. Methods Phys. Res., Sect. A **482**, 491 (2002).

[24] K. Chikanian, B. Kumar, N. Smirnov, and E. O'Brien, A momentum reconstruction algorithm for the PHENIX spectrometer at Brookhaven, Nucl. Instrum. Methods Phys. Res., Sect. A **371**, 480 (1996).

[25] M. Dasgupta, A. Fregoso, S. Marzani, and G. P. Salam, Towards an understanding of jet substructure, J. High Energy Phys. 09 (2013) 029.

[26] A. J. Larkoski, S. Marzani, G. Soyez, and J. Thaler, Soft drop, J. High Energy Phys. 05 (2013) 146.

[27] G. D'Agostini, Improved iterative Bayesian unfolding, in *Alliance Workshop on Unfolding and Data Correction* (2010), arXiv:1010.0632.

[28] L. Brenner, R. Balasubramanian, C. Burgard, W. Verkerke, G. Cowan, P. Verschuuren, and V. Croft, Comparison of

unfolding methods using RooFitUnfold, https://gitlab.cern.ch/RooUnfold/RooUnfold (2020).
[29] R. Brun, F. Bruyant, M. Maire, A. C. McPherson, and P. Zanarini, Geant3: User's guide Geant 3.10, Geant 3.11 (Rev. Version) (CERN, Geneva, 1987), https://cds.cern.ch/record/1119728.
[30] T. Sjostrand, S. Mrenna, and P. Z. Skands, PYTHIA6.4 physics and manual, J. High Energy Phys. 05 (2006) 026.
[31] S. S. Adler *et al.* (PHENIX Collaboration), Jet properties from dihadron correlations in $\mathrm{p+p}$ collisions at $\sqrt{s}=$ 200 GeV, Phys. Rev. D **74**, 072002 (2006).
[32] C. Bierlich *et al.*, A comprehensive guide to the physics and usage of PYTHIA8.3, SciPost Phys. Codebases **2022**, 8 (2022).
[33] P. Skands, S. Carrazza, and J. Rojo, Tuning PYTHIA8.1: The Monash 2013 tune, Eur. Phys. J. C **74**, 3024 (2014).
[34] J. Adam *et al.* (STAR Collaboration), Longitudinal double-spin asymmetry for inclusive jet and dijet production in pp collisions at $\sqrt{s}=510$ GeV, Phys. Rev. D **100**, 052005 (2019).
[35] S. Catani and M. H. Seymour, The dipole formalism for the calculation of QCD jet cross sections at next-to-leading order, Phys. Lett. B **378**, 287 (1996).
[36] S. Catani and M. H. Seymour, A general algorithm for calculating jet cross sections in NLO QCD, Nucl. Phys. **B485**, 291 (1997).
[37] J. Currie, E. W. N. Glover, and J. Pires, NNLO QCD predictions for single jet inclusive production at the LHC, Phys. Rev. Lett. **118**, 072002 (2017).
[38] M. Dasgupta, F. Dreyer, S. G. Salam, and G. Soyez, Small-radius jets to all orders in QCD, J. High Energy Phys. 04 (2015) 039.
[39] M. Dasgupta, F. Dreyer, S. Salam, and G. Soyez, Inclusive jet spectrum for small-radius jets, J. High Energy Phys. 06 (2016) 057.
[40] Summary of ATLAS PYTHIA8 tunes, https://cds.cern.ch/record/1474107/files/ATL-PHYS-PUB-2012-003.pdf (2012).
[41] G. Aad *et al.* (ATLAS Collaboration), Measurement of the Z/γ^{*} boson transverse momentum distribution in pp collisions at $\sqrt{s}=7$ TeV with the ATLAS detector, J. High Energy Phys. 09 (2014) 145.
[42] R. D. Ball *et al.*, Parton distributions with LHC data, Nucl. Phys. **B867**, 244 (2013).
[43] T. Gleisberg, S. Hoeche, F. Krauss, M. Schonherr, S. Schumann, F. Siegert, and J. Winter, Event generation with Sherpa 1.1, J. High Energy Phys. 02 (2009) 007.
[44] J. Bellm *et al.*, Herwig 7.2 release note, Eur. Phys. J. C **80**, 452 (2020).
[45] S. Acharya *et al.* (ALICE Collaboration), Charged jet cross section and fragmentation in proton-proton collisions at $\sqrt{s}=7$ TeV, Phys. Rev. D **99**, 012016 (2019).
[46] V. Khachatryan *et al.* (CMS Collaboration), Measurement of inclusive jet cross sections in pp and PbPb collisions at $\sqrt{s_{NN}}=2.76$ TeV, Phys. Rev. C **96**, 015202 (2017).
[47] CMS Collaboration, A Cambridge-Aachen(C-A) based jet algorithm for boosted top-jet tagging, Report No. CMS PAS JME-09-001, 2009, https://cds.cern.ch/record/1194489.
[48] A. M. Sirunyan *et al.* (CMS Collaboration), Measurement of the splitting function in $\mathrm{p+p}$ and $\mathrm{Pb+Pb}$ collisions at $\sqrt{s}=5.02$ TeV, Phys. Rev. Lett. **120**, 142302 (2018).
[49] J. Adam *et al.* (STAR Collaboration), Measurement of groomed jet substructure observables in $p+p$ collisions at $\sqrt{s}=200$ GeV with STAR, Phys. Lett. B **811**, 135846 (2020).
[50] M. S. Abdallah *et al.* (STAR Collaboration), Differential measurements of jet substructure and partonic energy loss in $\mathrm{Au+Au}$ collisions at $\sqrt{s}=200$ GeV, Phys. Rev. C **105**, 044906 (2020).
[51] R. Belmont, J. Brewer, Q. Brodsky, P. Caucal, and M. Connors, Predictions for the sPHENIX physics program, Nucl. Phys. **A1043**, 122821 (2022).
[52] https://www.hepdata.net/record/158374.

Correction: During the production process, the footnote to indicate deceased authors was applied to the wrong author name two times and has been fixed.